International Journal of Lightweight Materials and Manufacture 1 (2018) 142–156

Contents lists available at ScienceDirect

International Journal of Lightweight Materials and Manufacture

journal homepage: https://www.sciencedirect.com/journal/international-journal-of-lightweight-materials-and-manufacture

Original Article

Morphological evolution of GP zones and nanometer-sized precipitates in the AA2050 aluminium alloy

Tsai-Fu Chung [a], Yo-Lun Yang [b], Chien-Nan Hsiao [c], Wei-Chih Li [d], Bo-Ming Huang [a], Cheng-Si Tsao [a], Zhusheng Shi [b], Jianguo Lin [b], Paul E. Fischione [d], Takahito Ohmura [e], Jer-Ren Yang [a, *]

[a] Department of Materials Science and Engineering, National Taiwan University, Taipei, Taiwan
[b] Department of Mechanical Engineering, Imperial College London, London, SW7 2AZ, UK
[c] Instrument Technology Research Center, National Applied Research Lab, Hsinchu, Taiwan
[d] E.A. Fischione Instruments, Inc., 9003 Corporate Circle, Export, PA, 15632, USA
[e] National Institute for Materials Science, 1-2-1 Sengen, Tsukuba, Ibaraki, 305-0047, Japan

ARTICLE INFO

Article history:
Received 26 March 2018
Received in revised form
13 June 2018
Accepted 13 June 2018
Available online 3 July 2018

Keywords:
Cs-corrected HAADF-STEM
Al–Cu–Li (AA2050) aluminium alloy
GP(θ″) zones
T_1 precipitates
θ′ Precipitates
S precipitates

ABSTRACT

Cs-corrected high-angle-annular-dark-field scanning-transmission-electron microscopy (Cs-corrected HAADF-STEM) was employed to examine the phases in Al–Cu–Li alloy (AA2050), including GP(T_1), GP(θ″) and GPB zones with their subsequent nanometer-sized products, T_1 (Al_2CuLi), θ′ (Al_2Cu), and S (Al_2CuMg) precipitates, respectively. Under the peak-aging condition, some solute-atom enriched clusters could still be found, and the newly-formed nucleus of GP(θ″) with a mono-layer {100} plane of Cu atoms occurred at the adjacent area of the joint between θ′ and S precipitates or the edge of an individual S precipitate. The transition of a single Cu-layer GP(θ″) → θ′ was presumed to be transformation via in-situ nucleation. The developing GP(θ″) zones and θ′ precipitates were easily subjected to soft impingement. However, hard impingement between two variants of θ′ presumably occurred, wherein one θ′ variant precipitate was blocked out by the other θ′ variant. As for the creep-ageing forming (CAF) treated sample, some precipitates of T_1 and θ′ were found to have the cutting characteristic on specific ledges.

1. Introduction

2xxx series (Al–Cu–Li) aluminium alloys have widely been applied in the aerospace industry owing to their low density [1], high strength [2,3], and high fracture toughness [4,5]. In the AA2050 aluminium alloy, the additions of solute atoms such as Cu and Li atoms [6] induce the formation of T_1 (Al_2CuLi), θ′ (Al_2Cu), S (Al_2CuMg), and δ′ (Al_3Li) precipitates during the artificial ageing treatment [2,3,7–10]. However, the corresponding details of their evolutions have not been established. Previous investigations [7,8,11–15] indicated that the microstructural evolution of GP zones on different habit planes, i.e., GP(T_1) zones with $\{111\}_{Al}$ [7,15], GP(θ″) zones with $\{100\}_{Al}$ [8,11,12,16], and GPB zones with $\{120\}_{Al}$ [8,13,17], can respectively develop into T_1, θ′, and S precipitates. Furthermore, the nucleation sites of δ′ precipitates were supposed to form exactly along the $\{100\}_{Al}$ habit planes of GP(θ″) zones [9,14]. However, it is challenging to elucidate how GP(T_1), GP(θ″), and GPB zones develop from the different atomic planes of Al matrix. Although T_1 [7,15], θ′ [14,18], and δ′ [9,14] precipitates in the Al–Cu–Li alloy have been investigated by transmission electron microscopy (TEM) and the first principles calculation (Vienna Ab-initio Simulation Package, VASP), the detailed nucleation mechanism of θ′ precipitates has yet to be investigated. From TEM investigations [17–21], it has been suggested that even in peak-ageing or over-ageing treatments of Al-Cu-(Mg) [17,19,20], Al-Cu-Li [18], and Al–Zn–Mg [21] alloys, the solute atoms are still available for the formation of GP zones, which would coexist with other precipitates such as θ, θ′, and S precipitates in Al–Cu–Mg alloys [17,19,20]; T_1 and θ′ in the Al–Cu–Li alloy [18]; η′, η in the Al–Zn–Mg alloy [21]. Therefore, it is a good chance to examine the microstructural evolution of GP zones → T_1 or θ′ precipitates in

* Corresponding author.
E-mail address: jryang@ntu.edu.tw (J.-R. Yang).
Peer review under responsibility of Editorial Board of International Journal of Lightweight Materials and Manufacture.

https://doi.org/10.1016/j.ijlmm.2018.06.002

the present work. The T_1 precipitate [2,8,9,22] is recognized as having a plate-like morphology (with a high aspect ratio), a hexagonal structure, a space group P6/mmm, and a nominal composition of Al_2CuLi. From results obtained from X-ray and TEM diffraction patterns [23], convergent beam electron diffraction analysis (CBED) [24], and Cs-corrected high-angle-annular-dark-field scanning-transmission-electron-microscopy (Cs-corrected HAADF-STEM) [25], these previous works [23–25] reported that T_1 precipitates possessed the lattice parameters of a = 0.496 nm and c = 0.935 nm ~ 4d $(111)_{Al}$, where d $(111)_{Al}$ ~ 0.233 nm is the lattice spacing of the $(111)_{Al}$ plane. However, a recent investigation [26] proposed a new model of T_1 precipitates for different coordinates of atoms with the lattice parameters a = 0.496 nm and c = 1.418 nm. From the result of the related VASP calculation [26], this new model has claimed the modulation of the positions of Al atoms on the center plane and of Li atoms near the interfacial layers, leading to an energy state more stable than that in the previous model [23,24]. In addition, under the $[110]_{Al}$ and $[112]_{Al}$ zone axes, respectively, the Cs-corrected HAADF-STEM results [26] clearly indicated that Li atoms in the T_1 precipitate are positioned at the interfacial layers nearby the Al matrix, resulting in the expansion of the lattice constant of the c axis. The plate-like T_1 precipitates possess four variants on $\{\bar{1}11\}_{Al}$ habit planes [2,8,9], and their corresponding orientation relationships are listed in Table 1. Under TEM observation along the $[10\bar{1}0]_{T_1}//[110]_{Al}$ zone axis, two edge-on configurations (i.e., $T_1^{(2)}$ and $T_1^{(4)}$) are viewed as needle-like shapes, and their related orientation relationships with respect to the Al matrix can be expressed as: $(0001)_{T_1}//(1\bar{1}1)_{Al}$, $[10\bar{1}0]_{T_1}//[110]_{Al}$ and $(0001)_{T_1}//(1\bar{1}\bar{1})_{Al}$, $[10\bar{1}0]_{T_1}//[110]_{Al}$, respectively, as shown in Fig. 1. The other two variants of T_1 precipitates (i.e., $T_1^{(1)}$ and $T_1^{(3)}$) were observed as elliptical-like shapes along the $[10\bar{1}0]_{T_1}//[110]_{Al}$ zone axis, as illustrated in Fig. 1, similar to those of η′ precipitates in the Al–Zn–Mg aluminium alloy [27]. On the other hand, the plate-like θ′ precipitates were recognized as having a body-centered tetragonal (BCT) structure [9,28], a space group I4/m [28], a nominal composition of Al_2Cu [9,28], and lattice parameters of a = b = 0.404 nm, c = 0.580 nm [9,28]. θ′ precipitates supposedly possess three variants on $\{001\}_{Al}$ habit planes [9,28], and their corresponding orientation relationships with respect to the Al matrix are listed in Table 2. TEM observation along the $[001]_{\theta'}//[001]_{Al}$ zone axis revealed two variants of θ′ precipitates (i.e., $^{(2)}\theta'$ and $^{(3)}\theta'$) at edge-on configurations possessing the needle-like morphology, and the orientation relationships between θ′ precipitates and the Al matrix were expressed as: $(010)_{\theta'}//(010)_{Al}$, $[100]_{\theta'}//[100]_{Al}$ and $(100)_{\theta'}//(100)_{Al}$, $[010]_{\theta'}//[010]_{Al}$, respectively. The other variant of θ′ phases (i.e., $^{(1)}\theta'$) possessed the orientation relationship $(001)_{\theta'}//(001)_{Al}$, $[100]_{\theta'}//[100]_{Al}$ and appeared as a plate-like shape along the $[001]_{\theta'}//[001]_{Al}$ zone axis, as shown in the schematic diagram presented in Fig. 2. On the other hand, along the $[110]_{\theta'}//[110]_{Al}$ zone axis, one edge-on configuration of θ′ precipitates (i.e., $^{(1)}\theta'$) can be observed as illustrated in Fig. 1.

Previous works [9,14,18] reported that the δ′ precipitate, which nucleated along the plate-boundaries of GP(θ″) zones or θ′ precipitates, gradually developed into δ′/GP(θ″)/δ′ and δ′/θ′/δ′ layer-by-layer structures. Owing to the δ′ precipitate with the $L1_2$ structure [9], which is similar to the FCC structure of the Al matrix, it has been presumed that the δ′/GP(θ″)/δ′ and δ′/θ′/δ′ structures possess lower interfacial energies than those of the Al/GP(θ″)/Al and Al/θ′/Al structures, respectively [13,17].

Table 1
Four variants of T_1 precipitates.

T_1	Orientation relationship	
1	$(0001)_{T_1}//(111)_{Al}$	$[10\bar{1}0]_{T_1}//[\bar{1}10]_{Al}$
2	$(0001)_{T_1}//(1\bar{1}1)_{Al}$	$[10\bar{1}0]_{T_1}//[110]_{Al}$
3	$(0001)_{T_1}//(11\bar{1})_{Al}$	$[10\bar{1}0]_{T_1}//[\bar{1}10]_{Al}$
4	$(0001)_{T_1}//(1\bar{1}\bar{1})_{Al}$	$[10\bar{1}0]_{T_1}//[110]_{Al}$

From further investigations, the nucleation/transformation mechanisms of phases or precipitates should involve separated nucleation [21,29–34], sympathetic nucleation [18,35–41], and in-situ transformation [21,29,30,42–48]. After solute atomic clusters or metastable precipitates dissolve, the re-supersaturated solute atoms would rapidly enhance the nucleation of a new differently-structured precipitate elsewhere within the matrix; i.e., the so-called separated nucleation [29–34]. Two typical TEM examples are illustrated as follows. A TEM example displays a M_2C carbide forming after the Fe_3C dissolves in ferrite matrix of the Cr–Mo–C alloy steel [29,30]. Another TEM example indicates that the precipitation of η′ takes place after a GPII zone dissolves in Al matrix of the Al–Zn–Mg alloys [21]. On the other hand, as happens frequently in isothermal treatment, a subsequent newly-formed precipitate occurs at the interphase boundaries of the existing precipitate/matrix in some alloy systems [18,35–41]. This phenomenon is known as sympathetic nucleation. Previous works using optical micrographs (OM) and transmission electron microscopy (TEM) observations have provided several typical examples in the Fe–Mn–Si alloy steel [35,36], the Ti–Cr alloy [37,38], the Fe–Cr–Ni stainless steel [39], and the Al–Cu-(Li) alloy [18,41]. The investigation of sympathetic nucleation [35], first reported by Aaronson and Wells in 1956, indicated that the intra-granularly nucleated ferrite (α) formed at the existing ferrite/austenite (α/γ) interface in the Fe–Mn–Si alloy steel under the OM observation. As for the Ti–Cr alloy [37,38], the newly-formed α-Ti phase was supposedly caused by sympathetic nucleation. Furthermore, in the Fe–Cr–Ni stainless steel [39], the sympathetic nucleation of the newly-formed austenite (γ) at the broad interface of the existing austenite and ferrite matrix has been identified by TEM characterization. Importantly, it has been noticed that sympathetic nucleation and hard impingement are difficult to distinguish. Hard impingement occurs when the growing austenite comes into contact with another existing austenite. Therefore, due to extended heat treatment, the sympathetic nucleation configuration of the austenite could be misidentified by the hard impingement. This problem has also been reported in the investigation of the nucleation/growth of T_1 precipitates in the Al–Cu–Li alloy [18]. In this previous work under TEM observation along the $[110]_{Al}$ zone axis, it was difficult to confirm whether the joint of two variants of T_1 on $\{\bar{1}11\}_{Al}$ habit planes was caused by sympathetic nucleation or hard impingement. In addition, the growth of θ′ in the Al–Cu–Li alloy may stop before it contacts another existing variant of θ′; i.e., the so-called soft impingement. This phenomenon is presumed to be associated with the solute concentration distribution nearby the growing precipitate [48]. It is an unresolved question whether the nucleation of a newly-formed precipitate could occur at the interface of the existing precipitate/matrix, the former and the latter precipitates having different crystal structures. Finally, the in-situ nucleation/transformation [21,29–31,42–48] illustrates that the original precipitate is affected by the diffusion of solute-atoms and gradually develops into a new precipitate, which possesses a different composition and a different crystal structure. In Cr–C alloy steels, the in-situ nucleation/transformation can be illustrated by a typical example, the gradual replacement of M_3C carbide by M_7C_3 carbide in the ferrite matrix [30]. In the Al–Zn–Mg alloy, the transition of η′ ($Mg_2Zn_{5-x}Al_{2+x}$, x=2 to 4) → η ($MgZn_2$) caused by the diffusional Zn solute atoms is reported to be in-situ nucleation/transformation [21].

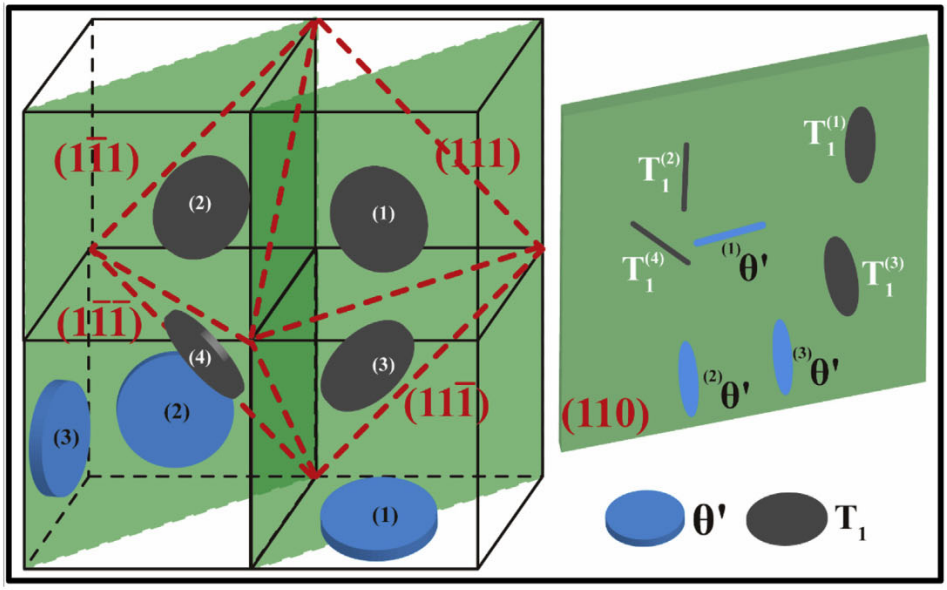

Fig. 1. T_1 precipitates are marked black; θ′, blue. Along the $[110]_{Al}$ zone axis, one θ′ (i.e., $^{(1)}\theta'$) and two T_1 (i.e., $T_1^{(2)}$ and $T_1^{(4)}$) precipitates appear with edge-on configurations along the $(001)_{Al}$, and $(1\bar{1}1)_{Al}$ and $(1\bar{1}\bar{1})_{Al}$ planes, respectively. The other variants of θ′ (i.e., $^{(2)}\theta'$ and $^{(3)}\theta'$) and T_1 (i.e.,$T_1^{(1)}$ and $T_1^{(3)}$) phases are without edge-on configuration.

Table 2
Three variants of θ′ precipitates.

θ′	Orientation relationship	
1	$(001)_{\theta'}//(001)_{Al}$	$[100]_{\theta'}//[100]_{Al}$
2	$(010)_{\theta'}//(010)_{Al}$	$[100]_{\theta'}//[100]_{Al}$
3	$(100)_{\theta'}//(100)_{Al}$	$[010]_{\theta'}//[010]_{Al}$

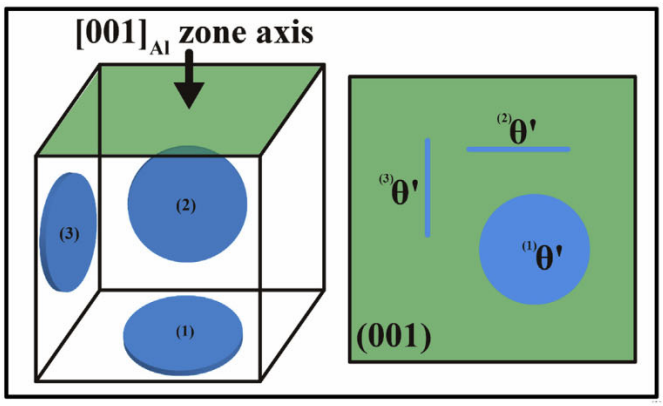

Fig. 2. Along the $[001]_{Al}$ zone axis, three variants of θ′ phases in the Al matrix: one variant (i.e., $^{(1)}\theta'$) is plate-like in shape, and two edge-on configurations (i.e., $^{(2)}\theta'$ and $^{(3)}\theta'$) are needle-like in shape.

In the Al–Cu–Li alloy, it has been reported that a single Cu-layer GP(θ″) zone gradually develops into θ′ (Al_2Cu) [16,18]. However, the corresponding nucleation mechanism remains to be confirmed. In addition, the formation of a single Cu-layer GP(θ″) zone [8,18] has yet to be investigated. It is apparent that the size and distribution of θ′ precipitates would be affected by the solute diffusion zone [48]. In the present work, the Cs-corrected HAADF-STEM investigations of GP zones, such as GP(T_1), GP(θ″), and GPB zones, and the subsequent precipitates, such as T_1, θ′, and S precipitates, were conducted. The nano-structural evolutions of GP zones and the subsequent precipitates have been explored. The mechanisms of the related nucleation with the phenomena of the soft and hard impingements of the precipitates will be addressed. In addition, the interaction between precipitates and dislocations in the AA2050 aluminium alloy is an intriguing subject for investigation. In this work, the cutting characteristics on ledges in T_1 and θ′ precipitates in samples treated by creep-age-forming (CAF) are reported.

2. Materials and methods

The chemical composition of the AA2050 aluminium alloy studied was Al-3.6Cu-0.9Li-0.34Mg-0.35Ag-0.34Mn-0.08Zr (wt.%). The thermal history of the as-received samples was solution treatment (at 500 °C for 1 h) followed by water quenching, and then the samples underwent a pre-strain (3.5–4.5%) process at room temperature. The as-received samples were treated with one-step ageing, conducted by heating to 155 °C and holding for 18 h (hereafter referred to as peak ageing samples, PA samples). In addition, the as-received alloy underwent creep-age forming (CAF), conducted by heating to 155 °C and holding for 18 h with simultaneously applied constant compression stress of 150 MPa (hereafter referred to as CAF samples).

The TEM specimens were prepared by cutting discs from PA samples and CAF samples (along their loading direction) and thinning the discs mechanically to 0.07 mm before they were twin-jet electropolished (using M110 Electro-polisher, E.A. Fischione Instruments) in a mixture of 33% nitric acid and 67% methanol at −25 °C with a working voltage of 12 V. To remove the oxidation layer introduced by the electrochemical process and further reduce sample thickness, the TEM foils were thinned by focus argon beam technique (using M1040 NanoMill, E.A. Fischione Instruments). A scanning, controllable argon beam with a beam size down to 1 μm can be targeted to a specific area of interest in the specimen to generate an amorphous-free, flat, and thin area for microstructure observations. Afterward, the specimen is treated by plasma cleaning to remove hydrocarbon contamination. The gas feed is about 5% oxygen, with the balance argon. In the plasma process (using Fischione M1070 Nanoclean plasma system), the downstream plasma dissociates oxygen molecules into oxygen radicals, reacting with the hydrocarbon contamination present on the surface of TEM

specimen, and finally forming carbon monoxide, carbon dioxide, and water. These gaseous species are then pumped away through the vacuum system of the instrument. The low-energy form of plasma enables effective cleaning with negligible specimen heating, ensuring that no phase transformation is induced during the plasma process.

An FEI Titan Chemi-STEM equipped with a spherical aberration corrector (Cs-corrector) achieves a ~1 Å probe size with beam current of ~70 pA, and a convergence semi-angle of ~19.8 mrad. The collecting angle of the HAADF detector was in the range of 7.9–42.8 mrad. The Cs-corrector HAADF-STEM micrograph provides the Z contrast image, which is proportional to Z^n, where n is close to 1.7–2 [14]. Since the atomic number of Cu (29) is higher than those of Al (13) and Li (3), the T_1 (Al_2CuLi) and θ′ (Al_2Cu) precipitates in the AA2050 aluminium alloy have significant differences in Z contrast in HAADF-STEM micrographs. The micrographs shown in the present study were raw images, without further image processing.

3. Results and discussion

In this work, HR-TEM/STEM micrographs (phase contrast/Z contrast images) for GP zones were performed as shown in Fig. 3. Fig. 3a displays an HR-TEM image along the $[110]_{Al}$ zone axis for the PA sample; two nano-scaled GP(T_1) zones in edge-on configurations of respective $(1\bar{1}1)_{Al}$ and $(1\bar{1}\bar{1})_{Al}$ habit planes can be observed. GP(T_1) zones have been presumed to serve as the precursors of T_1 precipitates, as they possess the same habit planes. In Fig. 3b, an HR-STEM image along the $[001]_{Al}$ zone axis for the PA sample, a single atomic layer of a GP(θ″) zone on the $(020)_{Al}$ habit plane can be identified; the GP(θ″) zone has been presumed to transform into the θ′ precipitate [16,18] for the subsequent ageing stages. In Fig. 3c, an HR-STEM image taken along the $[001]_{Al}$ zone axis for the CAF sample, a GPB zone on the $(2\bar{4}0)_{Al}$ habit plane, which is presumably the precursor of an S precipitate [8,13,17], can be observed.

As presented in the HR-STEM image of Fig. 3b, the GP(θ″) zone is supposedly composed of a single Cu-layer [8,16,18]. The copper atoms possess higher Z contrast atomic columns than the Al atoms. As presented in Fig. 3c for the GPB zone, which is expected to be Cu–Mg co-clusters forming along the $(2\bar{4}0)_{Al}$ habit plane [8,13,17], a Cu layer (with higher Z contrast) can be seen to be embraced by Mg atoms (with medium Z contrast, as compared with the lower Z contrast of Al atoms). The detailed nano-structural characterization of T_1, θ′, S, and δ′ precipitates will be presented below.

For the observation of the PA sample along the $[110]_{Al}$ zone axis, Fig. 4a displays a low-magnification BF-TEM micrograph (diffraction contrast image) of three precipitates in edge-on configurations of the respective $(1\bar{1}1)_{Al}$, $(1\bar{1}\bar{1})_{Al}$, and $(002)_{Al}$ habit planes. According to the orientation relationships of T_1 and θ′ precipitates, the

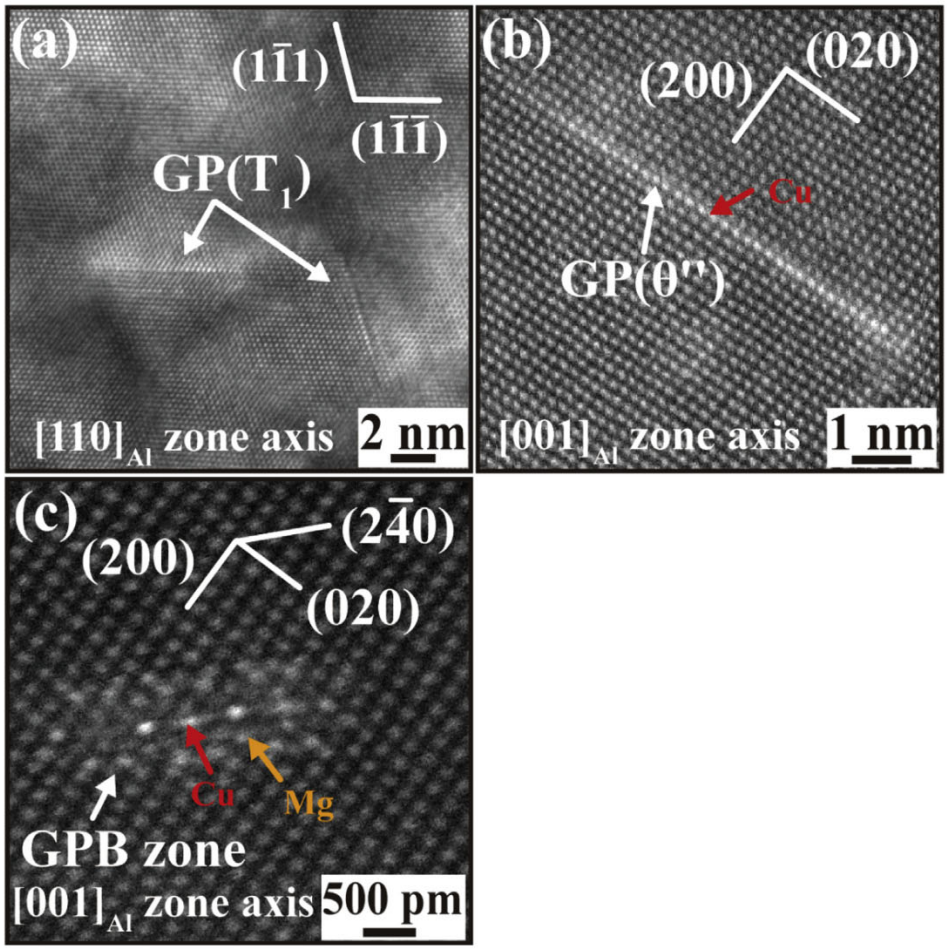

Fig. 3. (a) The HR-TEM image taken from the PA sample along the $[110]_{Al}$ zone axis, showing two GP(T_1) zones in edge-on configurations of $(1\bar{1}1)_{Al}$ and $(1\bar{1}\bar{1})_{Al}$ habit planes, respectively. (b, c) The HR-STEM images respectively taken from the PA and CAF samples, both along the $[001]_{Al}$ zone axis: (b) displaying a GP(θ″) zone consisting of a single Cu-layer (indicated as the red arrow) in the edge-on configuration of the $(020)_{Al}$ habit plane; (c) displaying a GPB zone composed of Cu and Mg atoms (indicated by the red and yellow arrows, respectively), forming on the $(2\bar{4}0)_{Al}$ habit plane.

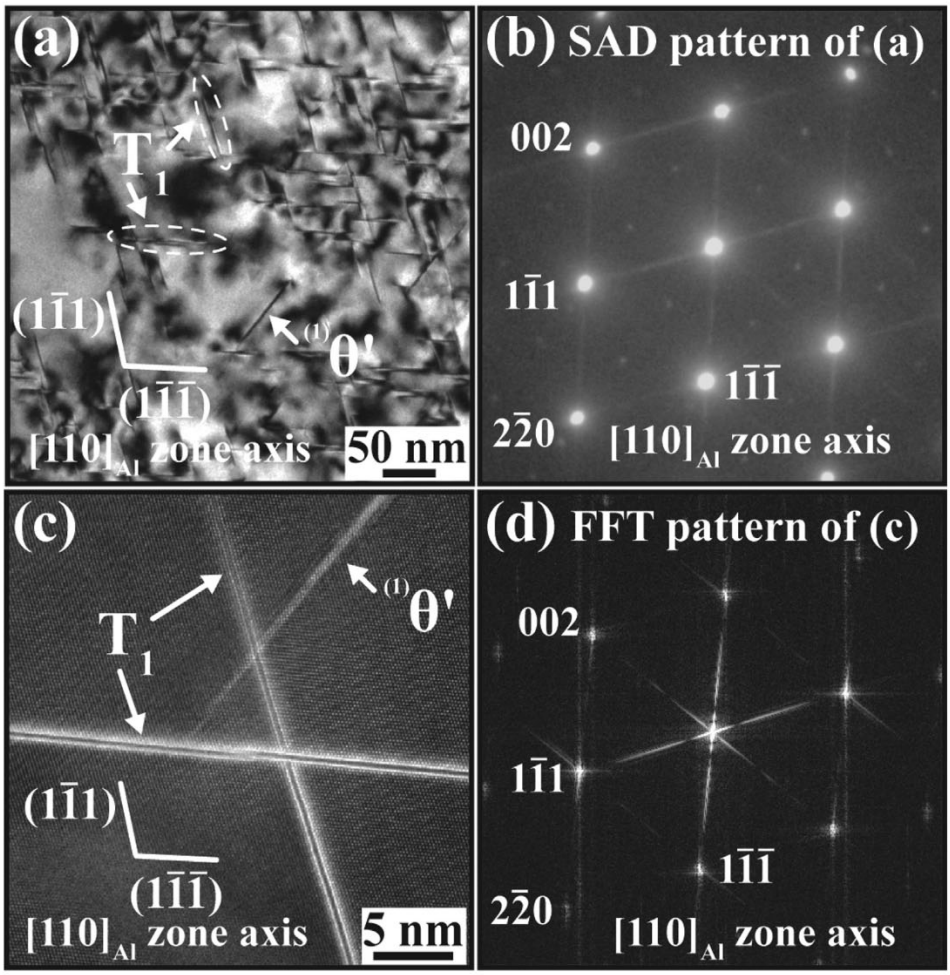

Fig. 4. The observation of the PA sample along the $[110]_{Al}$ zone axis. (a, b) The BF-TEM image with the corresponding SAD pattern showing that variants of T_1 brought about strong streaks along the $1\bar{1}1_{Al}$, and $1\bar{1}\bar{1}_{Al}$ poles, and satellite spots at 1/3 $2\bar{2}0_{Al}$; the thin θ′ growing on $(002)_{Al}$ habit planes led to the weak streaks along the 002_{Al} poles. (c, d) The HR-STEM image with the corresponding FFT diffractogram indicating that T_1 and θ′ precipitates were composed of different Z contrast layer-structures and the elongated streaks along the $1\bar{1}1_{Al}$, and $1\bar{1}\bar{1}_{Al}$ and 002_{Al} poles were caused by the high aspect ratios of T_1 and θ′ precipitates, growing on the $(1\bar{1}1)_{Al}$ and $(1\bar{1}\bar{1})_{Al}$ habit planes for T_1 and the $(002)_{Al}$ habit plane for θ′, respectively.

selected area diffraction (SAD) pattern, as illustrated in Fig. 4b, showed that the strong streaks along the $1\bar{1}1_{Al}$ and $1\bar{1}\bar{1}_{Al}$ poles arose from two edge-on configurations of T_1 precipitates growing on the $(1\bar{1}1)_{Al}$ and $(1\bar{1}\bar{1})_{Al}$ habit planes (i.e., $T_1^{(2)}$ and $T_1^{(4)}$ as portrayed in Fig. 1), and the satellite spots at 1/3 $2\bar{2}0_{Al}$ was caused by the non-edge-on configurations of T_1 precipitates growing on the $(111)_{Al}$ and $(11\bar{1})_{Al}$ habit planes (i.e., $T_1^{(1)}$ and $T_1^{(3)}$ as portrayed in Fig. 1). Notably, some weak streaks along the 002_{Al} poles can be recognized as θ′ precipitates that formed on the $(002)_{Al}$ habit plane, but their low intensity supposedly arose from the lower number density of θ′ with respect to that of T_1 in the Al matrix. These results of SAD patterns are similar to those of the investigations of Al–Li–Cu alloys [9,49]. Furthermore, in Fig. 4c, the high-magnification STEM micrograph (Z contrast images) under the $[110]_{Al}$ zone axis illustrated that two edge-on variants of T_1 precipitates on the $(1\bar{1}1)_{Al}$ and $(1\bar{1}\bar{1})_{Al}$ habit planes possessed the lower Z contrast inner-layers, sandwiched between two higher Z contrast outer-layers, and one variant of θ′ precipitates on the $(002)_{Al}$ habit plane was composed of the medium Z contrast inner-layers, framed by two lower Z contrast outer-layers. In Fig. 4d, owing to the plate-like T_1 and θ′ precipitates with high aspect ratios, their fast Fourier transformation (FFT) diffractograms revealed the streaking effect. The strong intensity of the streaking along the $1\bar{1}1_{Al}$ and $1\bar{1}\bar{1}_{Al}$ poles was supposedly caused by the higher number density of T_1 precipitates in the Al matrix. In contrast, θ′ precipitates provided the much weaker intensity of the streaking along the 002_{Al} pole.

In addition, the HR-STEM images shown in Fig. 4c indicated that some T_1 and θ′ precipitates apparently joined with each other; this phenomenon has also been reported in previous HR-TEM and 3D-APT (three-dimensional atom probe tomography) investigations [2,48,50,51]. The jointed area of T_1 precipitates is presumed to be the nucleation site for the formation of a new T_1 precipitate [50], which is supposed to be the sympathetic nucleation [18,35–41]. However, owing to the cross-section effects, two-dimensional (2D) TEM micrographs could not reveal the realistic relative positions between precipitates, such as three variants of θ′ reported in a previous investigation [48]. Therefore, it is unclear whether the joint of the intersected variants of T_1 was the nucleation site for new precipitates or the projection artefact forming a 2D image of a 3D TEM sample. This issue may possibly be resolved by three-dimensional (3D) tomography TEM with higher tilting angles.

Complementary to the orientation relationships of precipitates, HR-STEM micrographs and the corresponding FFT diffractograms in Fig. 5 were employed to identify these precipitates based on their atomic structures. The lattice images of T_1 and θ′ precipitates in the edge-on configurations of $(1\bar{1}\bar{1})_{Al}$ and $(002)_{Al}$ habit planes,

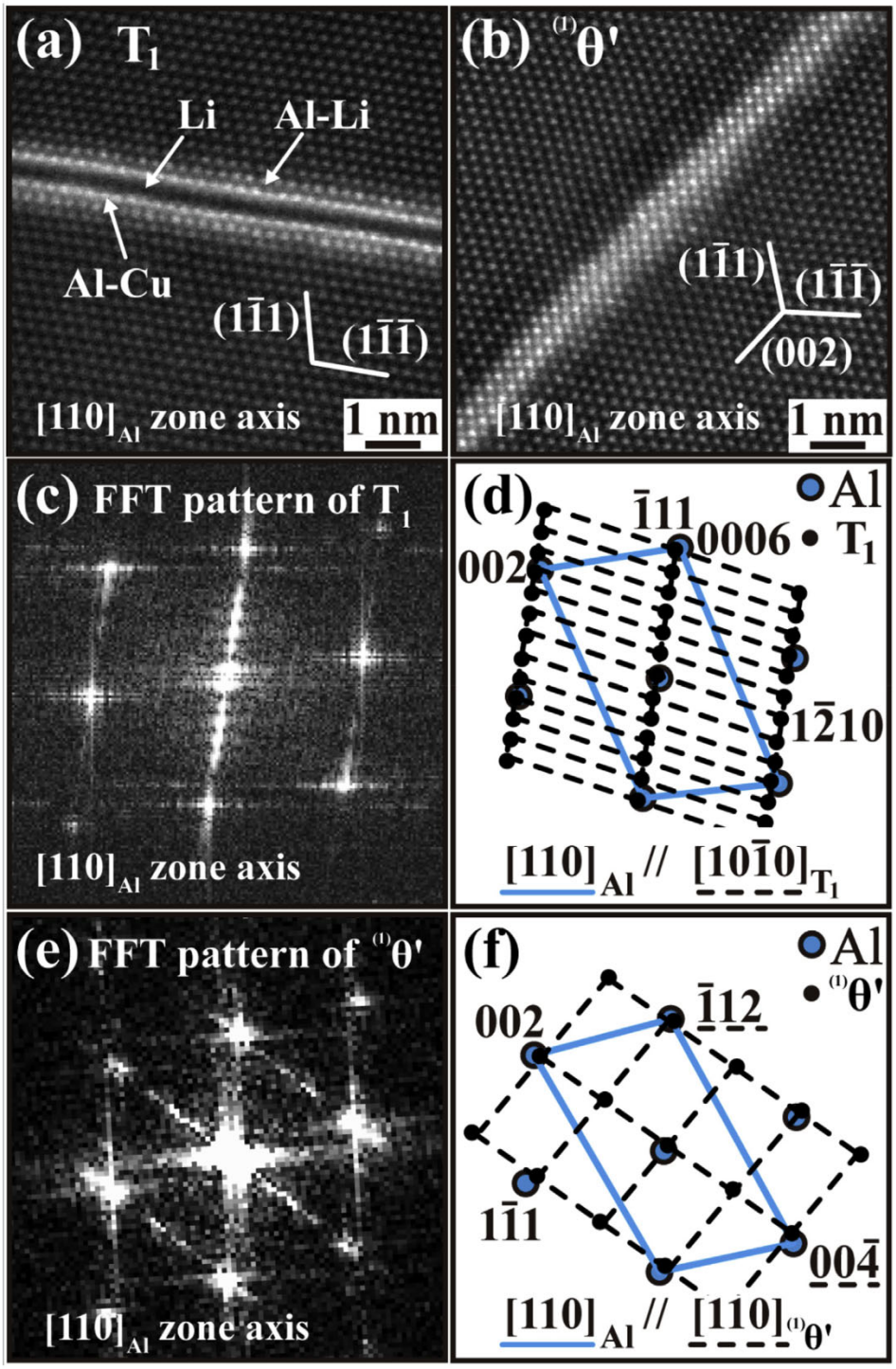

Fig. 5. The observation of the PA sample along the $[110]_{Al}$ zone axis. (a, b) The HR-STEM images showing the edge-on configurations of T_1 and θ′ precipitates on the $(1\bar{1}\bar{1})_{Al}$ and $(002)_{Al}$ habit planes, respectively. (c, d) Along the $[110]_{Al}//[10\bar{1}0]_{T1}$ zone axis, the FFT diffractogram and the simulated pattern of T_1 precipitate indicating the orientation relationship: $(0001)T_1//(1\bar{1}\bar{1})_{Al}$, $[10\bar{1}0]T_1//[110]_{Al}$. (e, f) Along the $[110]_{Al}//[110]_{\theta'}$ zone axis, the FFT diffractogram and the simulated diffraction pattern of θ′ precipitate indicating the orientation relationship: $(001)_{\theta'}//(001)_{Al}$, $[100]_{\theta'}//[100]_{Al}$.

respectively, illustrated the inward atomic arrangement. In Fig. 5a, the atomic imaging result of T_1 (Al_2CuLi) precipitates is consistent with that in the previous work [25], indicating the five symmetric layers, Al–Li/Al–Cu/Li/Al–Cu/Al–Li atomic layers, which have also been proposed based on Van Smaalen et al.'s model [52]. The outside layers, possessing diffused Z contrast of their atomic columns, are supposed to be the mixture of Al–Li atoms. The Al–Cu layers possess the highest contrast of their atomic columns because the atomic number of Cu (29) is higher than that of Al (13). Finally, the dark center layer shows that the lowest contrast of atomic columns is directly related to Li atoms. In Fig. 5b, the HR-STEM image taken along the $[110]_{Al}$ zone axis presents the $^{(1)}\theta'$ precipitate in the edge-on configuration of the $(002)_{Al}$ habit plane. The higher contrast layer of atomic columns within the center of the θ′

(Al_2Cu) precipitate is presumed to be the Cu-layer, and the decreasing contrast layer of atomic columns in the outer layer of the θ′ precipitates might be recognized as the Cu-solute depleted zones. Similar results have also been reported in previous investigations [14,48]. To reconfirm the T_1 and θ′ precipitates, their FFT diffractograms and the simulated diffraction patterns were associated with shapes and structures, and the orientation relationships with respect to the Al matrix are portrayed in Fig. 5c–d and 5e-f for T_1 and θ′ precipitates, respectively. Due to the effects of plate-like precipitate morphologies with high aspect ratios, the diffraction spots apparently had an elliptic intensity distribution. From the orientation relationship of T_1 and θ′ precipitates, under the $[10\bar{1}0]_{T_1}//[110]_{Al}//[110]_{\theta'}$ zone axis, the 0001_{T1} pole was parallel to the $\bar{1}11_{Al}$ pole, and the $002_{\theta'}$ spot, to the 002_{Al} pole.

The measurement of about 100 BF-TEM images of individual T_1 and θ′ precipitates revealed their lengths to be 73 ± 21 nm and 85 ± 40 nm, respectively, in the PA sample, and 57 ± 20 nm and 107 ± 42 nm, respectively, in the CAF sample. In addition, the thicknesses of T_1 and θ′ precipitates in the PA and the CAF samples were both smaller than 2 nm. It is suggested that creep age forming stress would influence the growth of T_1 and θ′ precipitates, but the related investigation is underway in this work. For illuminating the morphologies of precipitates, the lattice misfit calculations in conjunction with TEM have been found to be an effective means [21]. Two types of lattice misfits were determined on the $(0001)T_1//(1\bar{1}1)_{Al}$, and $(001)_{\theta'}//(001)_{Al}$ habit planes, respectively. One is vertical to the habit plane (i.e., δ(v)), in the thickness direction of the precipitate; the other is parallel to the habit plane (i.e., δ(p)), along the length direction of the precipitate. In addition, owing to the HCP structure of T_1 precipitates, δ(p) misfits should be estimated along two different close-packed directions: one parallel to the $[10\bar{1}0]$ direction (i.e., $\delta(p)[10\bar{1}0]$), and the other parallel to the $[11\bar{2}0]$ direction (i.e., $\delta(p)[11\bar{2}0]$) on the $(0001)T_1$ habit plane. For T_1 precipitates, the former misfit (δ(v)) was relatively larger:

$$|d(0001)_{T1} - 5\,d\left(1\bar{1}1\right)_{Al}| / 5\,d\left(1\bar{1}1\right)_{Al} = |(1.418 - 1.168)| / 1.168 \approx 21\%$$

whereas the latter two misfits ($\delta(p)[11\bar{2}0]$ and $\delta(p)[10\bar{1}0]$) were relatively small:

$$\delta(p)\left[11\bar{2}0\right] = |d\left(11\bar{2}0\right)_{T1} - 3\,d(121)_{Al}| / 3\,d(121)_{Al} = |(0.496 - 0.496)| / 0.496 = 0, \text{ and}$$

$$\delta(p)\left[10\bar{1}\,0\right] = |2\,d\left(10\bar{1}\,0\right)_{T1} - 3\,d(100)_{Al}| / 3\,d(100)_{Al} = |(0.859 - 0.858)| / 0.858 = 0.1\%,$$

where a = 0.496 nm, c = 1.418 nm for T_1 precipitates [26].

For θ′ precipitates, the former misfit (δ(v)) was much larger:

$$|d(002)_{\theta'} - 2\,d(002)_{Al}| / 2\,d(002)_{Al} = |(0.580 - 0.405)| / 0.405 \approx 43.2\%,$$

whereas the latter misfit (δ(p)[100]) was smaller:

$$|d(200)_{\theta'} - d(200)_{Al}| / d(200)_{Al} = |(0.404 - 0.405)| / 0.405 \approx 0.2\%,$$

where a = 0.404 nm, c = 0.580 nm for θ′ precipitates [9,28]. The results are consistent with a previous investigation [12] indicating that T_1 and θ′ precipitates possess plate-like morphologies with a higher aspect ratio and coherent board flat faces on the $(1\bar{1}1)_{Al}$ and $(1\bar{1}1)_{Al}$ habit planes for T_1 and the $(002)_{Al}$ habit plane for θ′, respectively.

As shown in Fig. 6, BF-TEM and HR-STEM images obtained from the CAF samples along the $[001]_{Al}$ zone axis displayed some characteristic features of precipitates. In Fig. 6a, the low-magnification BF-TEM micrograph indicates two edge-on configurations of θ′ precipitates (i.e., $^{(2)}\theta'$ and $^{(3)}\theta'$) on the respective $(020)_{Al}$ and $(200)_{Al}$ habit planes, and an edge-on configuration of S precipitate in the $(\bar{2}40)_{Al}$ habit plane. It was reported that cold-work forming before ageing treatment [53] or external stress during ageing treatment [54] would alter the lattice misfit of θ′ precipitates, probably resulting in the preferential growing orientation. Therefore, the dominant θ′-variant (i.e., $^{(2)}\theta'$) growing on the $(020)_{Al}$ habit plane would be related to the forming-stress of the CAF sample. From the corresponding SAD pattern, as illustrated in Fig. 6b, some streaks were parallel to the 020_{Al} pole arising from $^{(2)}\theta'$ precipitates on the $(020)_{Al}$ habit plane rather than the 200_{Al} pole, from $^{(3)}\theta'$ precipitates on the $(200)_{Al}$ habit plane. A previous investigation of the Al-1.3Cu (wt%) alloy [19] indicated that under the $[001]_{Al}$ zone axis, the face-on $^{(1)}\theta'$ precipitates on $(002)_{Al}$ habit planes (as indicated in Fig. 2) were attributable to the diffraction spots along 220_{Al}, 200_{Al} and 020_{Al} poles. In the present work for the CAF sample, it is suggested that the forming stress simultaneously eliminates the nucleation of θ′ precipitates on the $(002)_{Al}$ habit planes, resulting in the hardly observed diffraction spots of $^{(1)}\theta'$ precipitates. In addition, it was difficult to detect the spots contributed by the small fraction of S precipitates in the SAD pattern. The strong diffraction spots at $1/3\ 220_{Al}$, and $1/3\ 2\bar{2}0_{Al}$ resulted from the non-edge-on configurations of four variants of T_1 precipitates on the $\{111\}_{Al}$ habit planes. These SAD patterns are similar to those found in investigations of Al–Li–Cu alloys [9,49]. In Fig. 6c, two higher Z-contrast θ′ precipitates connected symmetrically with two adjacent lower Z-contrast layers, which are assumed to be the δ′ phase (as indicated with red arrows). This composite structure of δ′/θ′/δ′ has been proposed in previous investigations [9,14]; however, the nucleation mechanism between θ′ and δ′ precipitates has yet to be resolved. The FFT diffractograms of two variants of θ′ precipitates, as shown in Fig. 6d, similarly illustrated that the shape factor of plate-like morphologies with high aspect ratios would greatly elongate the diffraction spots along the 020_{Al} and 200_{Al} poles with respect to their $(020)_{Al}$ and $(200)_{Al}$ habit planes.

As shown in Fig. 7a and b, the magnified HR-STEM images obtained from the CAF samples along the $[001]_{Al}$ zone axis illustrated the atomic-scale characteristic features of θ′ and S precipitates. Two edge-on configurations of θ′ precipitates are supposed to be composed of Cu-rich layers (i.e., the higher Z-contrast) and framed by the symmetrical two adjacent δ′ phases (i.e., the lower Z-contrast), as illustrated in Fig. 7a. The similar composite structure of δ′/θ′/δ′ has been proposed in previous investigations [9,10,14,55,56]. In addition, the edge-on configuration of δ′ phases (Al_3Li), possessing the $L1_2$ structure (i.e., the FCC structure with Al atoms at the corners and Li atoms at the face centers), were aligned to the cubic-cubic orientation with respect to the Al matrix, characterized as $(010)_{\delta'}//(010)_{Al}$, $[001]_{\delta'}//[001]_{Al}$ [9]. It is apparent to observe δ′/θ′/δ′ structures rather than the δ′/T_1/δ′ or δ′/S/δ′ structures. The reason was supposed that the broad $\{100\}_{\theta'}$ planes, exactly comparable to $\{100\}_{\delta'}$ planes, would result in a lower nucleation energy, thereby easily becoming the nucleation site of δ′ phases [10]. Furthermore, according to a previous investigation [10], the attractive force between Cu and Li atoms is higher than that between Cu and Al. It could be suggested that the intrinsic Cu atoms of θ′ (Al_2Cu) possess the higher ability to trap Li atoms within the Al matrix; however, the abilities of the intrinsic Cu atoms of T_1 (Al_2CuLi) or S (Al_2CuMg) would be eliminated by Li and Mg atoms inward, respectively [10].

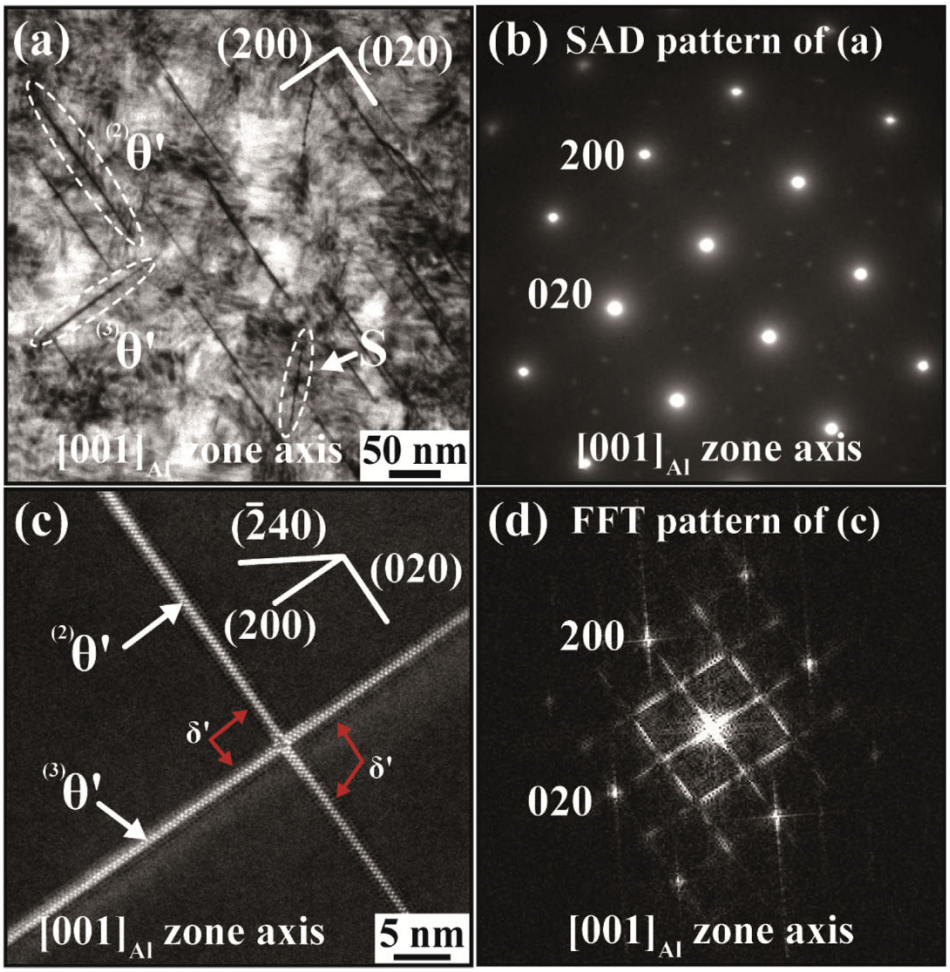

Fig. 6. The observation of the CAF sample along the $[001]_{Al}$ zone axis. (a) The BF-TEM image showing the edge-on configurations of $^{(2)}\theta'$ on the $(020)_{Al}$ habit planes, $^{(3)}\theta'$ on the $(200)_{Al}$ habit planes, and the S precipitate on the $(\bar{2}40)_{Al}$ habit planes. (b) The corresponding SAD patterns obtained from (a) showing the streaks along the 020_{Al} pole, which are caused by the variants of θ'; the satellite spots at 1/3 220_{Al} and 1/3 $2\bar{2}0_{Al}$, which are associated with four variants of T_1 precipitates. (c) The HR-STEM image showing that the higher Z contrast θ' precipitates ($^{(2)}\theta'$ and $^{(3)}\theta'$) are surrounded by the lower Z contrast δ' phases (red arrows). (d) The corresponding FFT diffractogram obtained from (c) showing the streaks respectively along the 020_{Al} and 200_{Al} poles due to the high aspect ratio of $^{(2)}\theta'$ and $^{(3)}\theta'$.

Moreover, two variants (i.e., $^{(2)}\theta'$ and $^{(3)}\theta'$) were joined to form a cross-shaped morphology under the observation along the $[001]_{Al}$ zone axis as shown in Fig. 7a. It is hard to explain the distorted atomic structure within the joint (as indicated by a yellow arrow). The chaotic structure was probably caused by the strain-field that occurred when $^{(2)}\theta'$ and $^{(3)}\theta'$ precipitates grew simultaneously. As the variant pairs of θ' were arrayed so symmetrically, this joint could probably have originated from sympathetic nucleation of θ' precipitates. In Fig. 7b, a striking HR-STEM image displays the morphology of the connected S-θ'-S structure: two S precipitates in the edge-on configuration of the $(\bar{2}40)_{Al}$ habit plane and a θ' precipitate in the edge-on configuration of the $(200)_{Al}$ habit plane. Previous works on the Al–Li–Cu alloy [8,13] reported that rod-like S precipitates with the orthorhombic structure possessed 12 complicated variants, and proposed that the general orientation relationships between S phase and aluminum matrix can be expressed as $(001)_S//(2\bar{1}0)_{Al}$, $[100]_S//[001]_{Al}$. For the observation of θ' precipitates under the $[001]_{Al}//[001]_{\theta'}$ zone axis, the $200_{\theta'}$ spot nearly overlapped the 200_{Al} spot (i.e., $d(200)_{\theta'} = 0.404$ nm $\approx d(200)_{Al} = 0.405$ nm), as portrayed in Fig. 7 c and d. For the S precipitate under the $[001]_{Al}//[100]_S$ zone axis, the 004_S spot is approximately parallel to the $2\bar{1}0_{Al}$ spot, as presented in Fig. 7e and f. Therefore, the identifications of θ' and S precipitates from FFT diffractograms and the simulated patterns according to the orientation relationships between precipitates and the Al matrix are of use.

The formation of θ' precipitates has been reported to develop from a single Cu-layer GP zone (i.e., GP(θ') zone) [16,18]. However, the nucleation mechanism of the GP(θ'') zone has not been clarified in detail, as mentioned in a previous investigation [18]. It was reported that after the natural ageing treatment, the isotropic distribution of the 2D small-angle X-ray scattering (SAXS) pattern revealed the existence of spherical particles in the Al matrix [18]. From the anomalous SAXS (ASAXS) measurements (i.e., the determination of the element composition according to its K_α-edge X-ray absorption), it can be concluded that these spherical precipitates appear to be rich in Cu atoms, named Cu-solute-clusters [18]. During the in-situ heating SAXS experiment from room temperature to 155 °C, the isotropic distribution of the 2D SAXS pattern apparently disappeared and then developed into the characteristic streaking 2D SAXS pattern [18]. It was supposedly caused by the dissolution of spherical Cu-solute-clusters, and then the formation of plate-like precipitates such as T_1 and θ' precipitates occurred. Furthermore, atomic-scale HR-STEM micrographs [14,16,18] indicated that the single Cu-layer GP zone would developed into θ' precipitates. Owing to the similar morphologies of the disk-like

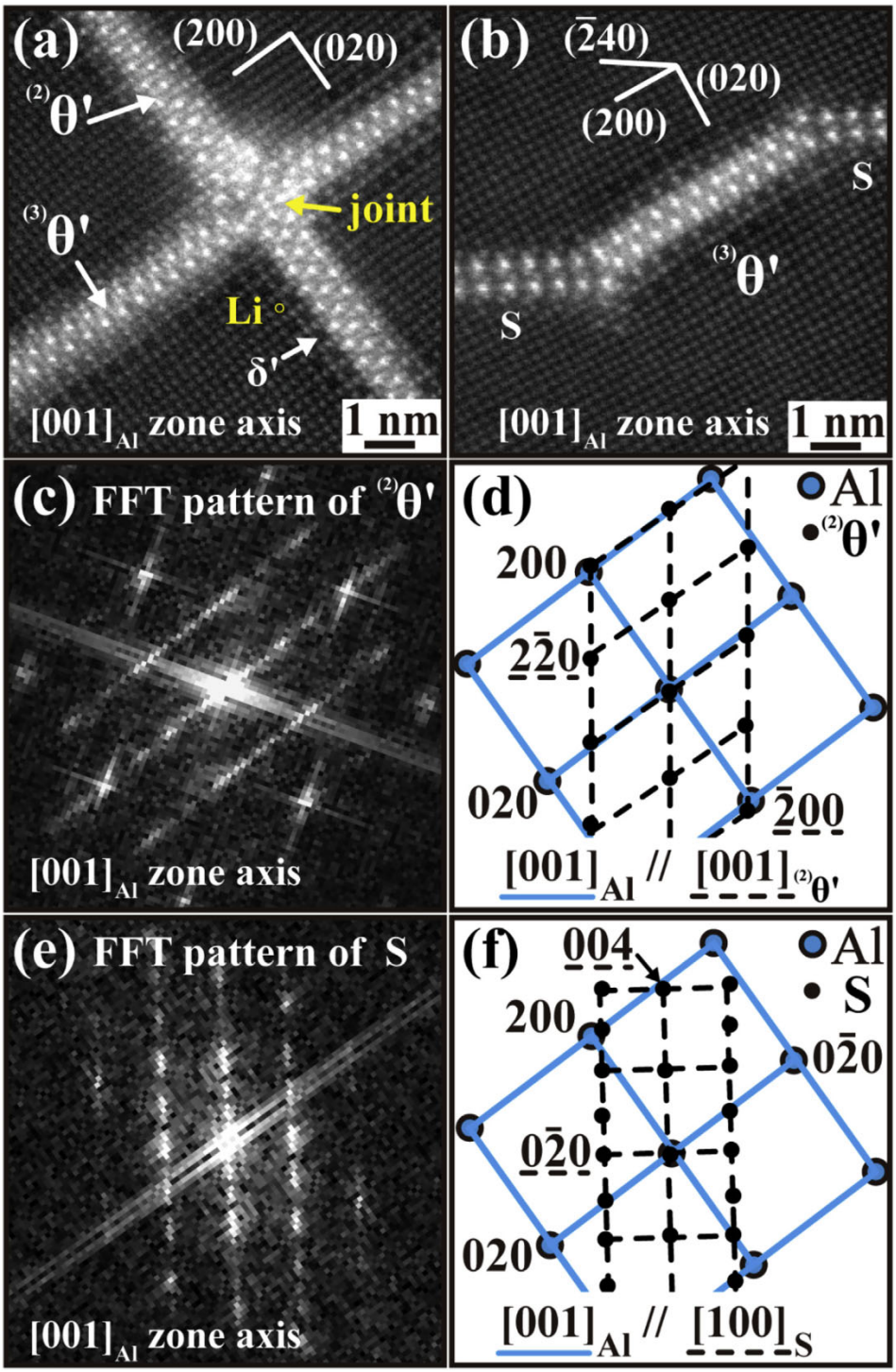

Fig. 7. The observation of the CAF sample along the $[001]_{Al}$ zone axis. (a) HR-STEM image showing that the joint of two edge-on configurations of θ′ surrounded by δ′, the latter possessing the square unit mesh of atomic arrangement of Li/Al. (b) HR-STEM image showing that the connected morphology of S-θ′-S structure. (c–d) The FFT diffractogram and the simulated diffraction pattern of θ′ precipitate with Al matrix indicating the orientation relationship: $(010)_{\theta'}//(010)_{Al}$, $[100]_{\theta'}//[100]_{Al}$. (e–f) The FFT diffractogram and the simulated diffraction pattern of S precipitate with Al matrix indicating the orientation relationship: $(001)_S//(2\bar{1}0)_{Al}$, $[100]_S//[001]_{Al}$.

single Cu-layer GP zones and the plate-like θ′ precipitates, it is difficult to use the reciprocal 2D SAXS pattern (i.e., the streaking distribution) to distinguish their respective transformation stages (i.e., single Cu-layer GP zone → θ′ precipitate). However, combining the ex-situ HR-STEM micrographs and the in-situ 2D SAXS pattern has confirmed that the single Cu-layer GP zone would occur after the dissolutions of Cu-solute-clusters [14,16,18]. In Fig. 8a and b, HR-STEM lattice images, taken from the CAF sample along the $[001]_{Al}$ zone axis, showed the Cu-solute-atom clusters adjacent to GP(θ″) zones; the former was supposed to be the precursor of the latter, which grew on the $(020)_{Al}$ habit plane. The remnant solute-clusters partially dissolved and gradually developed into GP(θ″) zones. This nucleation mechanism of GP(θ″) zones would be supposedly recognized as separated nucleation.

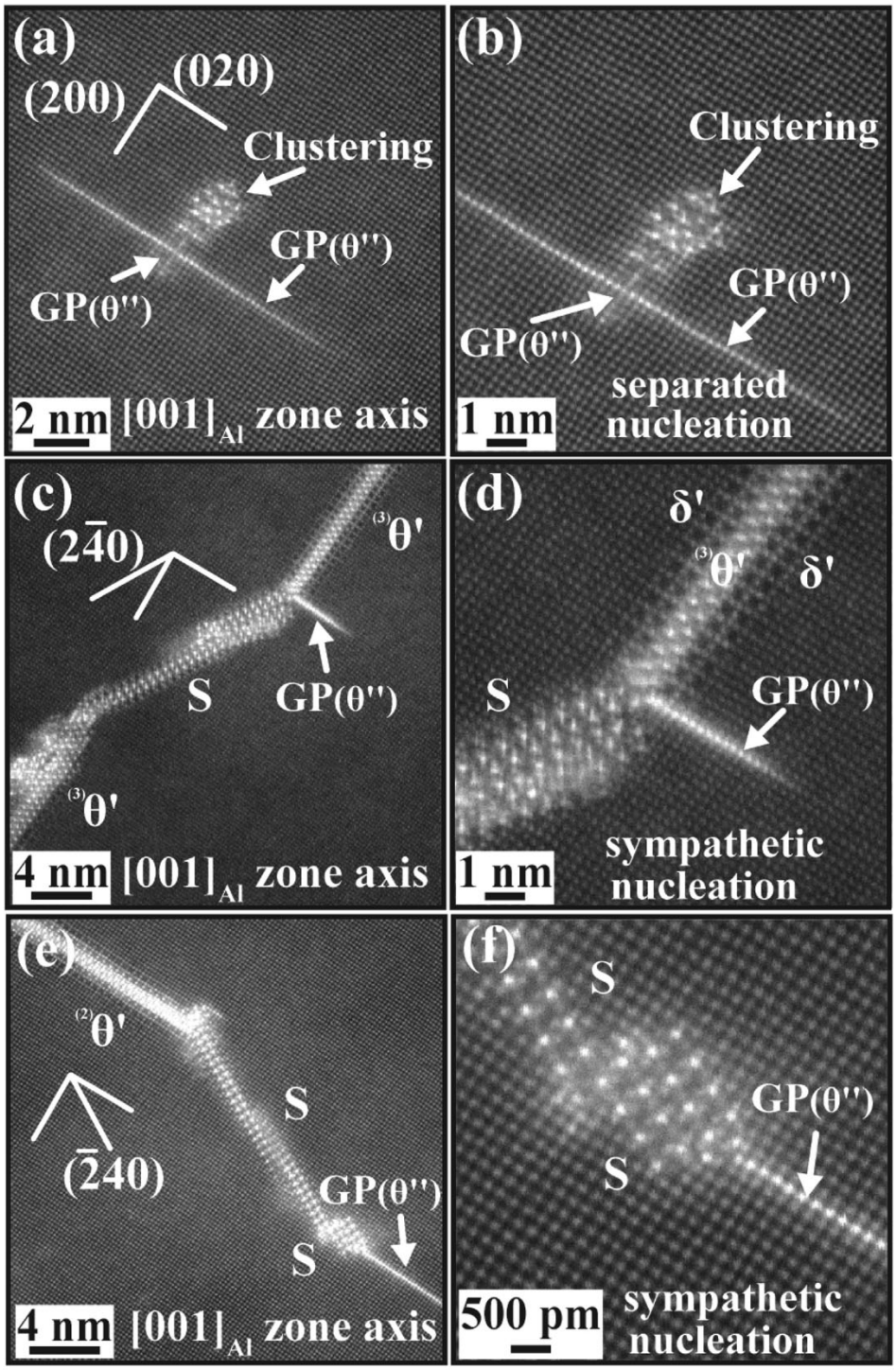

Fig. 8. The observation of the CAF sample along the $[001]_{Al}$ zone axis. (a, b) HR-STEM images showing the GP(θ″) adjacent to a solute-atom cluster, where this single Cu-layer GP(θ″), in the edge-on configuration on the $(020)_{Al}$ habit plane, was presumed to form via separated nucleation during the dissolution of this solute-atom cluster. (c, d) HR-STEM images probably showing the sympathetic nucleation of GP(θ″), where the GP(θ″) presumably nucleated on the joint of θ′ and S; (d) the enlarged HR-STEM obtained from (c). (e, f) probably showing the sympathetic nucleation of GP(θ″), where the single Cu-layer GP(θ″) was assumed to nucleate from the interface of the individual S precipitate; (f) the enlarged HR-STEM obtained from (e).

It is still unclear whether the nucleation of a newly-formed precipitate could occur at the interface of the existing precipitate/matrix, the former and the latter precipitates having different crystal structures. The HR-STEM lattice images in Fig. 8c and d shows that the S-precipitate, the θ′ precipitate and the GP(θ″) zone joined together to form a triple junction. The GP(θ″) zone growing on the $(200)_{Al}$ habit plane probably nucleated on the edge of θ′, which was with $(020)_{Al}$ habit plane. In fact, the newly nucleated GP(θ″) zone should be presumed to form from the interface boundary between the existing θ′ precipitate and aluminum matrix. The joint between θ′ and S precipitates probably provided the interface with the lower interfacial energy, thus

decreasing the nucleation energy barrier of the GP(θ″) zone. This nucleation mechanism is similar to the sympathetic nucleation reported previously [18,35–41], a newly-formed precipitate occurring at the interface of the existing precipitate with an identical structure. On the other hand, in Fig. 8e and f, the GP(θ″) zone nucleated on the interface of the individual S precipitate possessing a different phase structure from that of GP(θ″) zones. In this work, the creep age forming stress probably promoted a special mode of sympathetic nucleation, which occurs where the interface of the pre-existing S precipitate possesses a different phase structure of GP(θ″) zones. Whether the creep age forming stress might assist this type of sympathetic nucleation is still an unresolved question that should be elucidated. As the mechanism of the precipitate transformation involves the diffusion of atoms [14,18], it is difficult for θ′ to grow penetratingly through another θ′ or through the developed T_1, or S precipitates. In Fig. 7a, the joint of two θ′

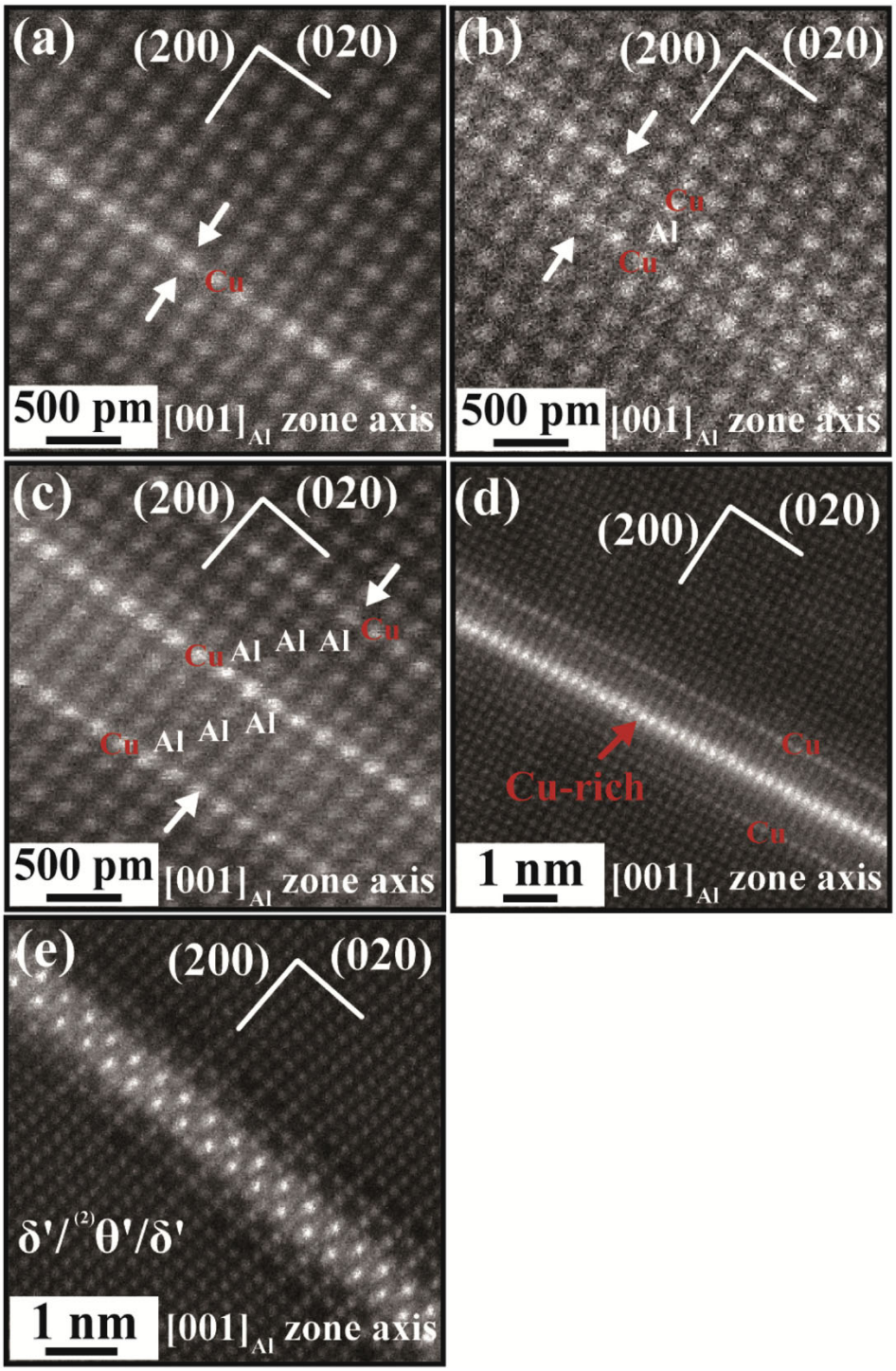

Fig. 9. The observation of different areas in the PA sample along the $[001]_{Al}$ zone axis. (a) HR-STEM image showing the single Cu-layer GP(θ″) in the edge-on configuration on $(020)_{Al}$ habit plane. (b, c) The single Cu-layer GP(θ″) transforming to three or five layers of GP(θ″), which consisted of one or three {010} planes of Al atoms. (d, e) The Cu-rich-layer GP(θ″) transforming to the θ′ precipitate, which possessed two Cu-layers, combining two adjacent δ′ precipitates to form a composite structure of δ′/θ′/δ′ precipitates.

precipitates is presumably due to sympathetic nucleation. The schematic representation of the possible sequence of events for sympathetic nucleation is portrayed in Supplementary Fig. 1.

Regarding θ′ precipitates, previous works on Al-Cu [28,57] and Al–Cu–Li [3,9,14] alloys have generally indicated the precipitation sequence of super-saturated solid solution → GP(θ″) zone → θ′ → θ. An intriguing phenomenon in the aluminium alloys is why, after artificial treatments, precipitates such as GP zones and stable precipitates can co-exist in the Al matrix of AA2xxx and AA7xxx series aluminium alloys [18–21]. In the work [19] from the BF-TEM images and the corresponding SAD patterns, it indicated that GPI zones co-existed with θ′ precipitates in the longer ageing time of the Al-1.3Cu (wt%) alloy aged at 130 °C for 18 days. The other work [20] claimed that after the Al-1.7Cu (wt%) alloy was under two-step ageing treatment, aged at 130 °C for 48h and then aged at 190 °C for 24h, GPI zones and GPII zones (i.e., θ″) would be observed in the Al matrix. In the investigation [21] of the Al-6.2Zn-2.1Mg-2.2Cu (wt%) alloy aged at 120 °C for 8h, at 165 °C for 1h, and then treated with creep-age forming (CAF) at 175 °C for 8h with an applied tensile stress of 162.5 MPa, the edge-on configurations of GPII zones, metastable precipitates (i.e., η′), and stable precipitates (i.e., η) on $\{111\}_{Al}$ habit planes in the Al matrix has been reported with HR-TEM images and the corresponding FFT diffractogram. Explicitly, these investigations showed that GP zones always exist within the whole ageing treatments of Al alloys. Therefore, it is a good chance to study the microstructure evolution of precipitates (GP zones→ metastable precipitates→ stable precipitates) in Al alloys of peak-ageing or over-ageing samples. In accordance with a previous investigation, the solid solubility of elements in aluminium [58], the solid solubility of Cu at 500 °C was approximately 2 wt%, and at 20 °C, below 0.1 wt%. The alloy, Al-3.6Cu-0.9Li-0.3 Mg (wt%) in this work, would produce the supersaturated content of Cu in the Al matrix after the solute treated condition. These supersaturated Cu atoms supposedly become Cu-clusters existing within the Al matrix [18], or CuMg-clusters accumulating near the dislocations or grain boundaries [2]. During the artificial ageing treatment, the majority of Cu-clusters [18] would induce the nucleation of GP zones, and parts of Cu-clusters would re-dissolve in the matrix. Accompanied by the partial dissolution of CuMg-clusters [2,18], it would lead to the super-saturation of Cu solute atoms in the Al matrix again, thereby enhancing the formation of GP zones. Therefore, it is a good chance to reveal the details of the microstructural evolution from GP(θ″) zone → θ′ precipitate in the present work. In Fig. 9, under the $[001]_{Al}$ zone axis, the HR-STEM micrographs were observed at different collected areas of the PA sample. Fig. 9a and b showed that the diffusional growth of the GP(θ″) zone progressed from a single Cu-layer GP(θ″) zone (i.e., highest Z contrast), the Cu atoms of which had taken the place of Al atoms on a $(020)_{Al}$ plane, toward 3 layers of the GP(θ″) zone, where two Cu layers on the $(020)_{Al}$ plane were separated by one (020) Al layer. Furthermore, 5 layers of the

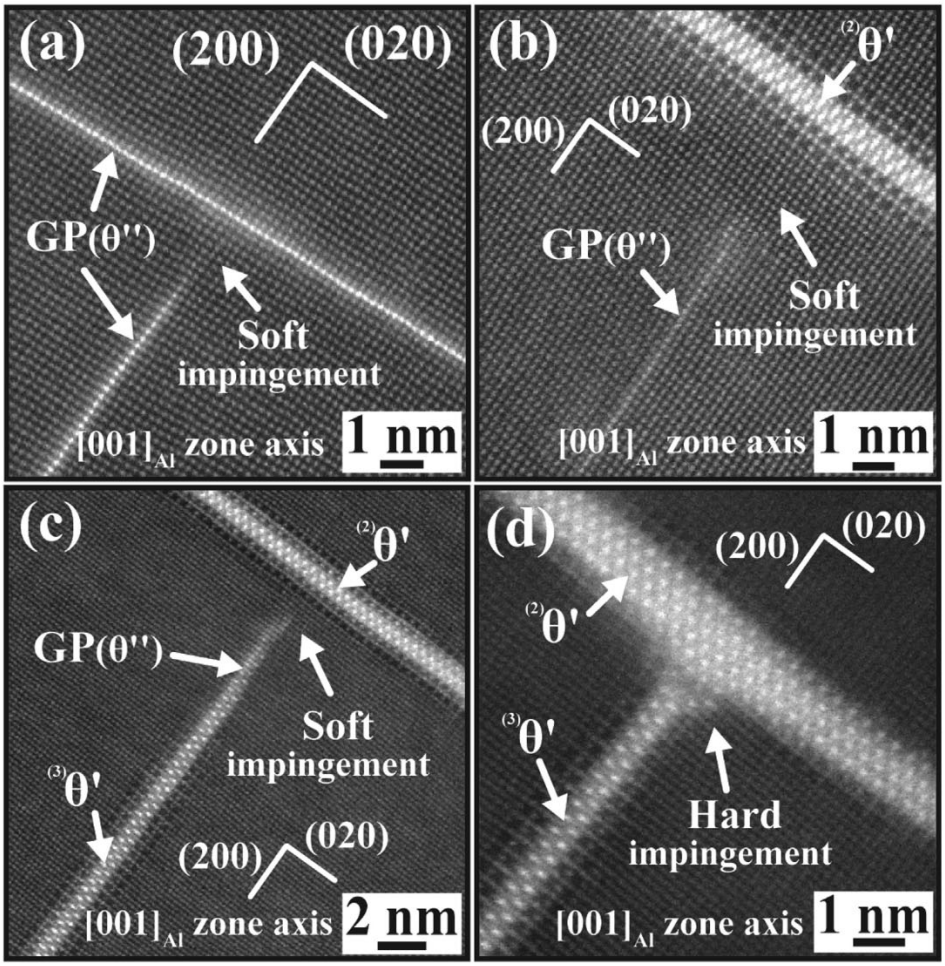

Fig. 10. The observation of PA and the CAF samples along the $[001]_{Al}$ zone axis. (a, b) HR-STEM images showing that a GP(θ″) precipitate was probably subjected to the soft impingement with respect to another GP(θ″) zone in (a) or θ′ precipitate in (b). (c, d) HR-STEM images showing that θ′ precipitates were very likely to be subjected to soft and hard impingements with respect to the other variants of θ′.

GP(θ″) zone could be observed in Fig. 9c, where two Cu layers on the $(020)_{Al}$ plane were separated by three (020) Al layers. In Fig. 9d, the Cu atoms had apparently accumulated in the central locus of the GP(θ″) zone, resulting in the coarsening of the Cu-atomic layer. Apart from the center of the GP(θ″) zone, the Z contrast gradually faded. In Fig. 9e, two Cu-layers developed into the θ′ precipitate, forming the composite structure of δ′/θ′/δ′ precipitates, which is frequently observed in PA and CAF samples.

The diffusional growth of the single Cu-layer GP(θ″) zone and the plate-like θ′ precipitates, which would be terminated by soft or hard impingement, affected the distance of closest approach between each variant of GP(θ″) zones and θ′ precipitates, thus altering the strengthening of precipitates reported in the developed work [48]. In this work, the PA and the CAF samples also demonstrated that both θ′ precipitates and the single Cu-layer GP(θ″) zones were subjected to soft or hard impingement, as shown in Fig. 10. After the nucleation of GP(θ″) zones (as illustrated in Fig. 8), the growth of one variant of GP(θ″) zones would easily be hindered by the other variant at soft impingement, as presented in Fig. 8a. It is presumable that the effect of soft impingement might be caused by the overlapping of the solute-depleted region [59] and postpone the growth of the GP(θ″) zone. In Fig. 10b, after the GP(θ″) zone → θ′ precipitate had already formed, the newly nucleated GP(θ″) zone would easily be subjected to soft impingement during the growth instead of hard impingement. On the other hand, during the growth of θ′ precipitates, soft impingement was also detected, as shown in Fig. 10c. Furthermore, hard impingement between two θ′ precipitates occurred, as shown in Fig. 10d. On the other hand, the phenomena of soft and hard impingement during the growth and coarsening of T_1 precipitates have been reported in a previous investigation [18], but it is usually difficult to distinguish between sympathetic nucleation and hard impingement. Some corresponding examples of T_1 precipitates are illustrated in Supplementary Fig. 2.

The yield strength evolution of Al–Cu–Li alloy, in the case of strengthening by T_1 precipitates, has been investigated using a model [60] for precipitate cutting, taking account of both interfacial and stacking-fault strengthening. It has been recognized that the main strengthening precipitate in Al–Cu–Li alloy is the T_1 phase of nominal composition Al_2CuLi, which forms extra-thin nano-platelets of high aspect ratio on the {111} planes of the Al matrix. The shearing of T_1 precipitates in a plastic deformed Al–Cu–Li alloy has been observed via HR-STEM images [61]; the cutting of T_1 precipitates has been proposed to be associated with single shearing events, supposedly related to a high energy cost of a second shear on the same slip plane. However, the relative displacement of the atomic planes due to cutting has not been estimated. In this work, HR-STEM investigation of the CAF sample also reveals the cutting of a T_1 precipitate, as shown in Fig. 11 a and b. Along $[110]_{Al}$ zone axis, the edge-on configuration of T_1 precipitate can be observed. From the atomic scale image (Fig. 11b), it is clear that during the process of creep-age-forming, the shearing of T_1 precipitates occurred. Two

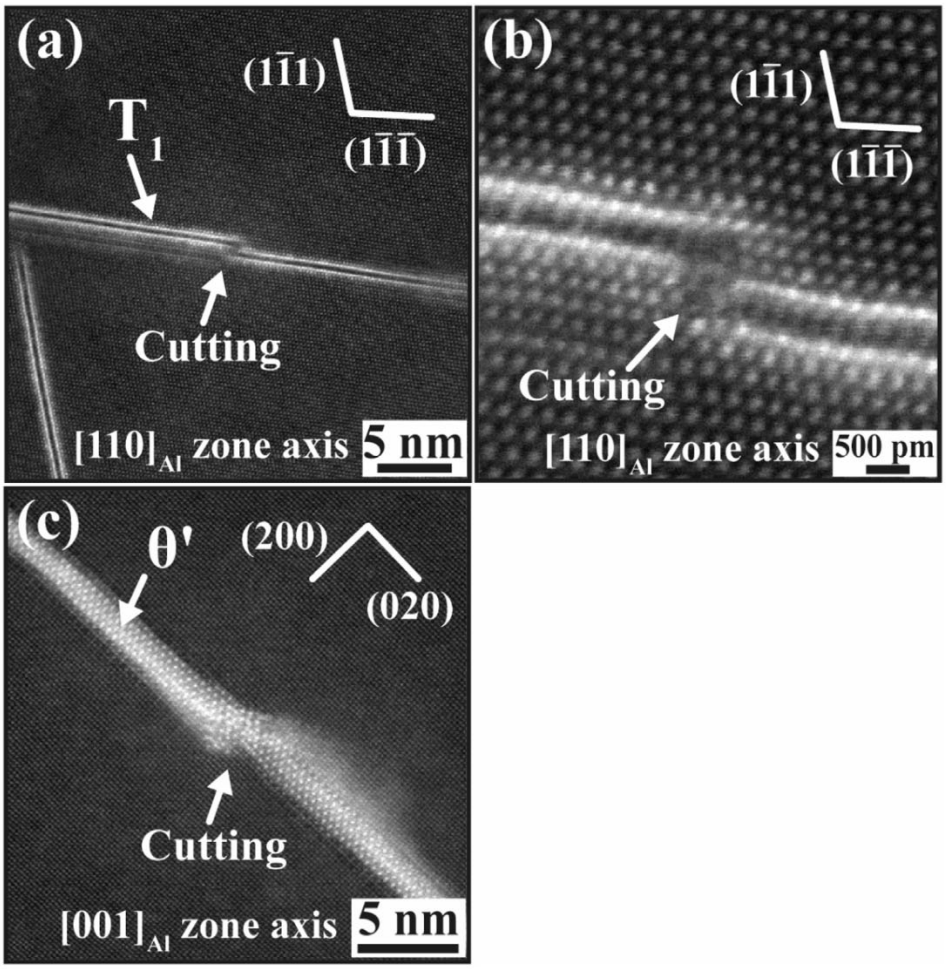

Fig. 11. The observation of the CAF sample along the respective $[110]_{Al}$ and $[001]_{Al}$ zone axes. (a, b) HR-STEM images showing the shearing on a T_1 precipitate. (b) The enlarged HR-STEM obtained from (a). (c) HR-STEM image showing the shearing on a θ′.

ledges of the new T_1/Al interface were created and probably resulted in a higher interfacial energy barrier for the movement of the subsequent dislocations. However, owing to the Li atom-columns (with the dark Z contrast) within the HR-STEM image of the T_1 precipitate, the amount of the cutting at the T_1/Al interface cannot be identified. In addition, the problem of a single cutting step or multiple cutting steps for the interaction between dislocation and T_1 has yet to be elucidated.

In previous works on the Al–Cu alloys [48,62–65] and an Al–Cu–Li alloy [14], the interaction between the dislocation and θ′ has been studied. The bowing and cutting mechanisms were evaluated according to the shear modulus of θ′ [62,66], the aspect ratio of the θ′ morphology [62], and slip band formation during the compression test [63]. However, the evidence for a possible mechanism is still lacking. The HR-STEM image (Fig. 11c) obtained from the CAF sample displays a shear deformation (cutting mechanism) on a θ′ precipitate. It has been suggested that the strong attractive strength between Cu and Li atoms [10] would apparently induce the formation of the coherent boundary on the $\{100\}_{\delta'}$//$\{100\}_{\theta'}$//$\{100\}_{Al}$ planes. The θ′ precipitate was surrounded with the δ′ phase (with the ordered lattice structure), thereby the δ′/θ′ interface resulting in a significant ability against dislocations [67]. In Fig. 11c, under the $[001]_{Al}$ zone axis, the image clearly indicates that the edge-on configuration θ′ precipitate (with a thickness of ~2.3 nm) was sheared by the dislocation on the specific glide plane, creating the ledges of the θ′/Al interface. The amount of cutting has yet to be investigated in detail.

4. Conclusions

In summary, Cs-corrected HAADF-STEM micrography clearly revealed the atomic-scale images of GP(T_1), GP(θ″), and GPB zones with the evolutions of nanometer-sized precipitates of T_1, θ′, and S in the peak-aging samples. The nucleation mechanism of the single Cu-layer GP(θ″) zones has been found to be sympathetic nucleation at the joint of θ′ precipitates adjacent to S precipitates or the edge of an individual S precipitate. The development of a single Cu-layer GP(θ″) → θ′ was ascribed to in-situ transformation. In addition, the development of GP(θ″) and θ′ precipitates is easily subjected to soft and hard impingement. In the creep ageing forming samples, the interactions between the dislocation and the precipitate (T_1 and θ′) were identified as the cutting mechanism.

Acknowledgement

This work was carried out with financial support from the Instrument Technology Research Center National Applied Research Lab, and the SMART Center of NTU-NIMS and Ministry of Science and Technology (Taiwan) under Contract MOST106-2923-E-002-009-MY2.

Appendix A. Supplementary data

Supplementary data related to this article can be found at https://doi.org/10.1016/j.ijlmm.2018.06.002.

References

[1] K. Kim, B.-C. Zhou, C. Wolverton, First-principles study of crystal structure and stability of T_1 precipitates in Al-Li-Cu alloys, Acta Mater. (2017) 337–346.
[2] V. Araullo-Peters, B. Gault, F.d Geuser, A. Deschamps, J.M. Cairney, Microstructural evolution during ageing of Al–Cu–Li–x alloys, Acta Mater. 66 (2014) 199–208.
[3] F.W. Gayle, F.H. Heubaum, J.R. Pickens, Structure and properties during aging of an ultra-high strength Al-Cu-Li-Ag-Mg alloy, Scripta Metall. Mater. 24 (1990) 79–84.
[4] K.S. Kumar, F.H. Heubaum, The effect of Li content on the natural aging response of Al-Cu-Li-Mg-Ag-Zr alloys, Acta Mater. 45 (1997) 2317–2327.
[5] Z. Chen, K. Zhao, L. Fan, Combinative hardening effects of precipitation in a commercial aged Al–Cu–Li–X alloy, Mater. Sci. Eng. A 588 (2013) 59–64.
[6] B.-P. Huang, Z.-Q. Zheng, Effects of Li content on precipitation in Al-Cu-(Li)-Mg-Ag-Zr alloys, Scripta Mater. 38 (1998) 357–362.
[7] Z. Gao, J.Z. Liu, J.H. Chen, S.Y. Duan, Z.R. Liu, W.Q. Ming, C.L. Wu, Formation mechanism of precipitate T_1 in AlCuLi alloys, J. Alloys Compd. 624 (2015) 22–26.
[8] S. Wang, M. Starink, Precipitates and intermetallic phases in precipitation hardening Al–Cu–Mg–(Li) based alloys, Int. Mater. Rev. 50 (2005) 193–215.
[9] R. Yoshimura, T.J. Konno, E. Abe, K. Hiraga, Transmission electron microscopy study of the evolution of precipitates in aged Al–Li–Cu alloys: the θ′ and T1 phases, Acta Mater. 51 (2003) 4251–4266.
[10] J. Howe, D. Laughlin, A. Vasudevan, A high-resolution transmission electron microscopy investigation of the δ'–θ'precipitate structure in an Al-2 wt% Li-1 wt% Cu alloy, Philos. Mag. A 57 (1988) 955–969.
[11] J.M. Galbraith, M.H. Tosten, P.R. Howell, On the nucleation of θ′ and T_1 on Al_3Zr precipitates in Al-Li-Cu-Zr alloys, J. Mater. Sci. 22 (1987) 27–36.
[12] A. Biswas, D.J. Siegel, C. Wolverton, D.N. Seidman, Precipitates in Al–Cu alloys revisited: atom-probe tomographic experiments and first-principles calculations of compositional evolution and interfacial segregation, Acta Mater. 59 (2011) 6187–6204.
[13] H. Djaaboube, D. Thabet-Khireddine, TEM diffraction study of Al_2CuMg (S′/S) precipitation in an Al–Li–Cu–Mg (Zr) alloy, Phil. Mag. 92 (2012) 1876–1889.
[14] S.Y. Duan, C.L. Wu, Z. Gao, L.M. Cha, T.W. Fan, J.H. Chen, Interfacial structure evolution of the growing composite precipitates in Al-Cu-Li alloys, Acta Mater. 129 (2017) 352–360.
[15] Y. Deng, J. Bai, X. Wu, G. Huang, L. Cao, L. Huang, Investigation on formation mechanism of T_1 precipitate in an Al-Cu-Li alloy, J. Alloys Compd. 723 (2017) 661–666.
[16] C. Liu, S.K. Malladi, Q. Xu, J. Chen, F.D. Tichelaar, X. Zhuge, H.W. Zandbergen, In-situ STEM imaging of growth and phase change of individual $CuAl_X$ precipitates in Al alloy, Sci. Rep. 7 (2017) 1–8.
[17] S. Ringer, T. Sakurai, I. Polmear, Origins of hardening in aged Al-Cu-Mg-(Ag) alloys, Acta Mater. 45 (1997) 3731–3744.
[18] B. Decreus, A. Deschamps, F. De Geuser, P. Donnadieu, C. Sigli, M. Weyland, The influence of Cu/Li ratio on precipitation in Al–Cu–Li–x alloys, Acta Mater. 61 (2013) 2207–2218.
[19] V.A. Phillips, High resolution electron microscope observations on precipitation in Al-3.0% Cu alloy, Acta. Metall. Mater 23 (1975) 751–767.
[20] G. Greetham, R. Honeycombe, The deformation of single crystals of aluminium 4.5-percent copper alloy, J. Inst. Met. 89 (1960) 13–21.
[21] T.-F. Chung, Y.-L. Yang, B.-M. Huang, Z. Shi, J. Lin, T. Ohmura, J.-R. Yang, Transmission electron microscopy investigation of separated nucleation and in-situ nucleation in AA7050 aluminium alloy, Acta Mater. 149 (2018) 377–387.
[22] B.I. Rodgers, P.B. Prangnell, Quantification of the influence of increased pre-stretching on microstructure-strength relationships in the Al–Cu–Li alloy AA2195, Acta Mater. 108 (2016) 55–67.
[23] J. Huang, A. Ardell, Crystal structure and stability of T_1, precipitates in aged Al–Li–Cu alloys, Mater. Sci. Technol. 3 (1987) 176–188.
[24] K.S. Vecchio, D.B. Williams, Convergent beam electron diffraction analysis of theT_1 (Al_2CuLi) phase in Al-Li-Cu alloys, Metall. Trans. A 19 (1988) 2885–2891.
[25] P. Donnadieu, Y. Shao, F. De Geuser, G.A. Botton, S. Lazar, M. Cheynet, M. de Boissieu, A. Deschamps, Atomic structure of T_1 precipitates in Al–Li–Cu alloys revisited with HAADF-STEM imaging and small-angle X-ray scattering, Acta Mater. 59 (2011) 462–472.
[26] C. Dwyer, M. Weyland, L.-Y. Chang, B. Muddle, Combined electron beam imaging and ab initio modeling of T_1 precipitates in Al–Li–Cu alloys, Appl. Phys. Lett. 98 (2011) 201909.
[27] W. Yang, S. Ji, M. Wang, Z. Li, Precipitation behaviour of Al–Zn–Mg–Cu alloy and diffraction analysis from η′ precipitates in four variants, J. Alloy. Comp. 610 (2014) 623–629.
[28] L. Bourgeois, C. Dwyer, M. Weyland, J.-F. Nie, B.C. Muddle, Structure and energetics of the coherent interface between the θ′ precipitate phase and aluminium in Al–Cu, Acta Mater. 59 (2011) 7043–7050.
[29] H.K.D.H. Bhadeshia, R. Honeycombe, Steels: Microstructure and Properties, third ed., Butterworth-Heinemann, 2011.
[30] J. Yang, C. Huang, C. Yang, J. Horng, Microstructural examination of 2.25Cr-1Mo Steel Steam pipes after extended service, Mater. Char. 30 (1993) 75–88.
[31] H. Löffler, I. Kovács, J. Lendvai, Decomposition processes in Al-Zn-Mg alloys, J. Mater. Sci. 18 (1983) 2215–2240.
[32] A. Inoue, T. Masumoto, Carbide reactions ($M_3C \rightarrow M_7C_3 \rightarrow M_{23}C_6 \rightarrow M_6C$) during tempering of rapidly solidified high carbon Cr-W and Cr-Mo steels, Metall. Trans. A 11 (1980) 739–747.
[33] D. Raynor, J. Whiteman, R. Honeycombe, Precipitation of molybdenum and vanadium carbides in high-purity iron alloys, Iron Steel Inst J 204 (1966) 349–354.
[34] S. Ringer, K. Hono, I. Polmear, T. Sakurai, Nucleation of precipitates in aged Al-Cu-Mg-(Ag) alloys with high Cu:Mg ratios, Acta Mater. 44 (1996) 1883–1898.
[35] H. Aaronson, C. Wells, Sympathetic nucleation of ferrite, Trans. Am. Inst. Min. Metall. Eng. 8 (1956) 1216–1223.

[36] H.I. Aaronson, G. Spanos, R.A. Masamura, R.G. Vardiman, D.W. Moon, E.S.K. Menon, M.G. Hall, Sympathetic nucleation: an overview, Mat. Sci. Eng. B 32 (1995) 107–123.
[37] E.S.K. Menon, H.I. Aaronson, Overview no. 57 Morphology, crystallography and kinetics of sympathetic nucleation, Acta. Metall. Mater 35 (1987) 549–563.
[38] T. Furuhara, J.M. Howe, H.I. Aaronson, Interphase boundary structures of intragranular proeutectoid α plates in a hypoeutectoid Ti-Cr alloy, Acta Metall. Mater. 39 (1991) 2873–2886.
[39] C.Y. Chen, H.W. Yen, J.R. Yang, Sympathetic nucleation of austenite in a Fe–22Cr–5Ni duplex stainless steel, Scripta Mater. 56 (2007) 673–676.
[40] J.M. Rosalie, L. Bourgeois, Silver segregation to θ′ (Al_2Cu)–Al interfaces in Al–Cu–Ag alloys, Acta Mater. 60 (2012) 6033–6041.
[41] J.M. Rosalie, L. Bourgeois, B.C. Muddle, Precipitation of the Θ′(Al2Cu) Phase in Al-cu-ag Alloys, Light Metals, Springer, 2012, pp. 307–312.
[42] K. Kuo, C. Jia, Crystallography of $M_{23}C_6$ and M_6C precipitated in a low alloy steel, Acta. Metall. Mater 33 (1985) 991–996.
[43] D. Raynor, J. Whiteman, R. Honeycombe, In-situ transformation of Fe_3C to Mo_2C in iron-molybdenum-carbon alloys, Iron Steel Inst J 204 (1966) 1114–1116.
[44] D.V. Shtansky, K. Nakai, Y. Ohmori, Mechanism and crystallography of ferrite precipitation from cementite in an Fe-Cr-C alloy during austenitization, Philos. Mag. A 79 (1999) 1655–1669.
[45] A. Inoue, S. Arakawa, T. Masumoto, In situ transformation of cementite to M_7C_3 and Internal defects of M_7C_3 in high carbon-chromium steel by tempering, Trans. Jpn. Inst. Met 19 (1978) 11–17.
[46] C.-S. Tsao, E.W. Huang, M.-H. Wen, T.-Y. Kuo, S.-L. Jeng, U.S. Jeng, Y.-S. Sun, Phase transformation and precipitation of an Al–Cu alloy during non-isothermal heating studied by in situ small-angle and wide-angle scattering, J. Alloy. Comp. 579 (2013) 138–146.
[47] M. Gazizov, R. Kaibyshev, The precipitation behavior of an Al–Cu–Mg–Ag alloy under ECAP, Mater. Sci. Eng. A 588 (2013) 65–75.
[48] J. da Costa Teixeira, D.G. Cram, L. Bourgeois, T.J. Bastow, A.J. Hill, C.R. Hutchinson, On the strengthening response of aluminum alloys containing shear-resistant plate-shaped precipitates, Acta Mater. 56 (2008) 6109–6122.
[49] A. Deschamps, M. Garcia, J. Chevy, B. Davo, F. De Geuser, Influence of Mg and Li content on the microstructure evolution of AlCuLi alloys during long-term ageing, Acta Mater. 122 (2017) 32–46.
[50] W.A. Cassada, G.J. Shiflet, E.A. Starke, Mechanism of Al_2CuLi (T_1) nucleation and growth, Metall. Trans. A 22 (1991) 287–297.
[51] B. Gault, F. de Geuser, L. Bourgeois, B.M. Gabble, S.P. Ringer, B.C. Muddle, Atom probe tomography and transmission electron microscopy characterisation of precipitation in an Al–Cu–Li–Mg–Ag alloy, Ultramicroscopy 111 (2011) 683–689.
[52] S. Van Smaalen, A. Meetsma, J.L. De Boer, P.M. Bronsveld, Refinement of the crystal structure of hexagonal Al_2CuLi, J. Solid State Chem 85 (1990) 293–298.
[53] S.P. Ringer, B.C. Muddle, I.J. Polmear, Effects of cold work on precipitation in Al-Cu-Mg-(Ag) and Al-Cu-Li-(Mg-Ag) alloys, Metall. Mater. Trans. A 26 (7) (1995) 1659–1671.
[54] T. Eto, A. Sato, T. Mori, Stress-oriented precipitation of G.P. Zones and θ′ in an Al-Cu alloy, Acta. Metall. Mater 26 (3) (1978) 499–508.
[55] E. Gumbmann, W. Lefebvre, F. De Geuser, C. Sigli, A. Deschamps, The effect of minor solute additions on the precipitation path of an Al-Cu-Li alloy, Acta Mater. 115 (2016) 104–114.
[56] M. Tosten, A. Vasudevan, P. Howell, The aging characteristics of an Al-2 Pct Li-3 Pct Cu-0.12 Pct Zr alloy at 190° C, Metall. Trans. A 19 (1) (1988) 51–66.
[57] Y. Chang, Crystal structure and nucleation behavior of {111} precipitates in an Al-3.9Cu-0.5Mg-0.5Ag alloy (PhD Thesis), Materials Science and Engineering, Carnegie Mellon University, Pittsburgh, 1993.
[58] I.J. Polmear, Physical Metallurgy of Aluminium Alloys, Chapter 2, Light Alloys, Butterworth-Heinemann, Oxford, 2006, pp. 29–96.
[59] L. Xu, D. Zhang, Y. Liu, B. Ning, Z. Qiao, Z. Yan, H. Li, Precipitation kinetics of $M_{23}C_6$ in T/P92 heat-resistant steel by applying soft-impingement correction, J. Mater. Res. 28 (11) (2013) 1529–1537.
[60] T. Dorin, A. Deschamps, F.D. Geuser, C. Sigli, Quantification and modelling of the microstructure/strength relationship by tailoring the morphological parameters of the T1 phase in an Al–Cu–Li alloy, Acta Mater. 75 (2014) 134–146.
[61] A. Deschamps, B. Decreus, F. De Geuser, T. Dorin, M. Weyland, The influence of precipitation on plastic deformation of Al–Cu–Li alloys, Acta Mater. 61 (2013) 4010–4021.
[62] J. da Costa Teixeira, L. Bourgeois, C.W. Sinclair, C.R. Hutchinson, The effect of shear-resistant, plate-shaped precipitates on the work hardening of Al alloys: towards a prediction of the strength–elongation correlation, Acta Mater. 57 (2009) 6075–6089.
[63] C.S. Kaira, C. Kantzos, J.J. Williams, V. De Andrade, F. De Carlo, N. Chawla, Microstructural evolution and deformation behavior of Al-Cu alloys: a Transmission X-ray Microscopy (TXM) and micropillar compression study, Acta Mater. 144 (2018) 419–431.
[64] J.F. Nie, B.C. Muddle, Strengthening of an Al–Cu–Sn alloy by deformation-resistant precipitate plates, Acta Mater. 56 (2008) 3490–3501.
[65] G. Liu, Time-resolved and three-dimensional study of dislocation-particle interactions in aluminum and copper alloys (PhD Thesis), University of Illinois at Urbana-Champaign, 2011.
[66] A. Pattnaik, A. Lawley, Deformation and fracture in Al–$CuAl_2$ eutectic composites, Metal. Mater. Transact. B 2 (1971) 1529–1536.
[67] B.C. Lee, J.K. Park, Effect of the addition of Ag on the strengthening of Al3Li phase in Al–Li single crystals, Acta Mater. 46 (12) (1998) 4181–4187.